

THE CO-TO-H₂ CONVERSION FACTOR FROM INFRARED DUST EMISSION ACROSS THE LOCAL GROUP

ADAM K. LEROY^{1,11}, ALBERTO BOLATTO², KARL GORDON³, KARIN SANDSTROM⁴, PIERRE GRATIER⁵, ERIK ROSOLOWSKY⁶,
 CHARLES W. ENGELBRACHT⁷, NORIKAZU MIZUNO⁸, EDVIGE CORBELLI⁹, YASUO FUKUI¹⁰, AND AKIKO KAWAMURA¹⁰

¹ National Radio Astronomy Observatory, Charlottesville, VA 22903, USA

² Department of Astronomy, University of Maryland, College Park, MD 20742, USA

³ Space Telescope Science Institute, Baltimore, MD 21218, USA

⁴ Max-Planck-Institut für Astronomie, D-69117 Heidelberg, Germany

⁵ Laboratoire d'Astrophysique de Bordeaux, Université de Bordeaux, OASU, CNRS/INSU, 33271 Floirac, France

⁶ University of British Columbia Okanagan, Kelowna, BC V1V 1V7, Canada

⁷ Steward Observatory, University of Arizona, Tucson, AZ 85721, USA

⁸ National Astronomical Observatory of Japan, 2-21-1 Osawa, Mitaka, 181-8588 Tokyo, Japan

⁹ INAF-Osservatorio Astrofisico di Arcetri, 50125 Firenze, Italy

¹⁰ Department of Astrophysics, Nagoya University, Furocho, Chikusaku, Nagoya 464-8602, Japan

Received 2010 September 21; accepted 2011 February 21; published 2011 July 22

ABSTRACT

We estimate the conversion factor relating CO emission to H₂ mass, α_{CO} , in five Local Group galaxies that span approximately an order of magnitude in metallicity—M 31, M 33, the Large Magellanic Cloud (LMC), NGC 6822, and the Small Magellanic Cloud (SMC). We model the dust mass along the line of sight from infrared (IR) emission and then solve for the α_{CO} that best allows a single gas-to-dust ratio (δ_{GDR}) to describe each system. This approach remains sensitive to CO-dark envelopes H₂ surrounding molecular clouds. In M 31, M 33, and the LMC we find $\alpha_{\text{CO}} \approx 3\text{--}9 M_{\odot} \text{ pc}^{-2} (\text{K km s}^{-1})^{-1}$, consistent with the Milky Way value within the uncertainties. The two lowest metallicity galaxies in our sample, NGC 6822 and the SMC ($12 + \log(\text{O}/\text{H}) \approx 8.2$ and 8.0), exhibit a much higher α_{CO} . Our best estimates are $\alpha_{\text{CO}}^{\text{NGC6822}} \approx 30 M_{\odot} \text{ pc}^{-2} (\text{K km s}^{-1})^{-1}$ and $\alpha_{\text{CO}}^{\text{SMC}} \approx 70 M_{\odot} \text{ pc}^{-2} (\text{K km s}^{-1})^{-1}$. These results are consistent with the conversion factor becoming a strong function of metallicity around $12 + \log(\text{O}/\text{H}) \sim 8.4\text{--}8.2$. We favor an interpretation where decreased dust shielding leads to the dominance of CO-free envelopes around molecular clouds below this metallicity.

Key words: dust, extinction – galaxies: ISM – ISM: clouds – ISM: molecules – Local Group

Online-only material: color figures

1. INTRODUCTION

In the local universe, stars form out of clouds made of molecular hydrogen (H₂; e.g., Fukui & Kawamura 2010). Understanding the processes that lead to star formation on large scales requires measuring the mass and distribution of this gas. Unfortunately, H₂ lacks a dipole moment, most molecular gas is found under conditions too cold to excite quadrupole emission, and the high opacity of molecular clouds prevents UV absorption studies from probing the bulk of the gas. Estimates of a galaxy's H₂ distribution therefore rely on indirect tracers, most commonly the lower rotational transitions of CO. The conversion between CO intensity and H₂ abundance has been the topic of a great deal of investigation. In particular, the effect of metallicity and the local radiation field on the CO-to-H₂ mass conversion factor, α_{CO} ,¹² have been studied for more than two decades.

Infrared (IR) dust emission is a powerful tool to address this problem. Dust is observed to be well mixed with gas (e.g., Bohlin et al. 1978; Boulanger et al. 1996) and may be mapped by its emission at IR wavelengths (e.g., Schlegel et al. 1998). By comparing IR emission, CO, and H I, one can constrain α_{CO} (e.g., Thronson 1988; Israel 1997b). The procedure is to estimate the dust mass from IR emission, measure atomic gas (H I) and

CO emission over a matched area, and then assume that the total gas mass (H₂ + H I) is proportional to the dust mass, with the two related by a fixed gas-to-dust ratio. With measurements that span a range of relative CO, H I, and dust masses, it is possible to simultaneously constrain the gas-to-dust ratio and α_{CO} . Key advantages of this approach are that it remains sensitive to any CO-free envelopes of H₂ and that the calibration of α_{CO} is pinned to the H I within the system being studied.

This exercise has been applied to several dwarf irregular galaxies (Israel 1997a, 1997b; Leroy et al. 2007, 2009; Gratier et al. 2010; A. Bolatto et al. 2011, in preparation). In the low-metallicity Small Magellanic Cloud (SMC), the results suggest a very large $\alpha_{\text{CO}} \sim 90\text{--}270 M_{\odot} \text{ pc}^{-2} (\text{K km s}^{-1})^{-1}$. An analogous application to the Milky Way yields $\alpha_{\text{CO}} \sim 4\text{--}9 M_{\odot} \text{ pc}^{-2} (\text{K km s}^{-1})^{-1}$ (Bloemen et al. 1990; Dame et al. 2001), roughly compatible with determinations of α_{CO} from fitting the diffuse γ -ray background (Strong & Mattox 1996; Abdo et al. 2010).

Most studies of α_{CO} have focused on a single galaxy or high latitudes in the Milky Way, where confusion is minimal. Israel (1997b) worked with a varied galaxy sample but since his work the available IR and CO data for nearby galaxies have improved dramatically. This is largely thanks to the *Spitzer Space Telescope*, which recently finished its cool mission and produced high-quality maps of a number of Local Group galaxies. This is therefore a natural time to apply this technique to measure α_{CO} across the Local Group in a self-consistent way.

In this paper, we combine maps of CO, H I, and IR emission to estimate α_{CO} in five Local Group galaxies: the massive spiral M 31, the dwarf spiral M 33, the dwarf irregular NGC 6822, and

¹¹ Hubble Fellow.

¹² We work with α_{CO} , the conversion from integrated CO intensity to mass of molecular gas. A linear scaling relates α_{CO} to X_{CO} , the conversion from integrated CO intensity to column density of H₂. Including helium, $X_{\text{CO}} \text{ cm}^{-2} (\text{K km s}^{-1})^{-1} = 4.6 \times 10^{19} \alpha_{\text{CO}} M_{\odot} \text{ pc}^{-2} (\text{K km s}^{-1})^{-1}$.

the Large Magellanic Cloud (LMC), and the SMC. By treating all five systems self-consistently, we minimize uncertainty in the “zero point” of the approach. With the *Herschel* mission now underway and the execution of several complementary CO and H I surveys, this approach should be readily extensible to many nearby galaxies in the next few years.

2. THE MODEL

We assume that dust and gas are linearly related by a gas-to-dust ratio, δ_{GDR} , so that

$$\delta_{\text{GDR}} \Sigma_{\text{dust}} = \Sigma_{\text{H}_2} + \Sigma_{\text{H I}}, \quad (1)$$

where Σ_{dust} , Σ_{H_2} , and $\Sigma_{\text{H I}}$ are the mass surface densities of dust, H_2 , and H I along a line of sight. Substituting $\Sigma_{\text{H}_2} = \alpha_{\text{CO}} I_{\text{CO}}$, we have

$$\delta_{\text{GDR}} \Sigma_{\text{dust}} = \alpha_{\text{CO}} I_{\text{CO}} + \Sigma_{\text{H I}}, \quad (2)$$

where the CO-to- H_2 conversion factor, α_{CO} , and gas-to-dust ratio, δ_{GDR} , are unknown and Σ_{dust} , I_{CO} , and $\Sigma_{\text{H I}}$ are measured. After assembling Σ_{dust} , I_{CO} , and $\Sigma_{\text{H I}}$ over many lines of sight in a region, we will use these data to solve for α_{CO} that best allows a single δ_{GDR} to describe the data.

2.1. α_{CO} : Definitions and Scales

The literature contains several working definitions of α_{CO} that apply to different scales or phases of the gas. In this paper and Equation (2), we define α_{CO} as the factor to convert from CO emission to *total* molecular gas mass on scales larger than individual clouds. Under this definition, α_{CO} includes any H_2 associated with C^+ in the outer, poorly shielded parts of clouds as well as gas immediately mixed with CO. Indeed, our goal is to measure whether such envelopes become dominant below some metallicity. Because this definition integrates over cloud structure, it is possible to derive a single α_{CO} for a whole galaxy or part of a galaxy, and to view that α_{CO} as a function of large-scale environmental factors. We choose this definition of α_{CO} because it is directly applicable to CO measurements of distant galaxies on kiloparsec scales.

This is distinct from the ratio of CO to H_2 only for molecular gas mixed with CO. Dynamical measurements using CO emission at high spatial resolution may mainly probe this quantity with limited sensitivity to H_2 in an extended envelope not mixed with CO. The difference between this quantity and the quantity that we study has caused some confusion, leading to apparent contradictions between IR-based measurements and dynamical measurements. In fact, these may be largely attributed to the different regions being probed (Section 6).

Similarly, we do *not* define α_{CO} as the ratio of H_2 to CO along a pencil beam. We have no reason to expect that this quantity, or any ratio that places many elements across a cloud, remains reasonably constant across part of a galaxy. In contrast, comparisons of dust and CO emission imply dramatic variations in the CO-to- H_2 ratio within individual clouds (Pineda et al. 2008).

Our spatial resolution ranges from 45 to 180 pc (Table 1). For these resolutions, giant molecular clouds (GMCs) will mostly lie within one or two resolution elements (e.g., Heyer et al. 2009). This is ideal for our definition of α_{CO} . We wish to integrate over the structure of these clouds to make a single α_{CO} a more appropriate assumption.

Table 1
Targets

System	Metallicity ^a 12 + log(O/H)	Resolution	
		($''$)	(pc)
M 31			
Inner	9.0	45	170
North	8.7	45	170
South	8.7	45	170
M 33			
Inner	8.33	45	180
Outer	8.27	45	180
LMC	8.43	240	60
NGC 6822	8.2	45	110
SMC			
West	8.02	156	45
East	8.02	156	45
North	8.02	156	45

^a **References.** (M 31) Yin et al. 2009 (compilation); (M 33) Rosolowsky & Simon 2008; (LMC and SMC) Dufour 1984; Keller & Wood 2006; (NGC 6822) Israel 1997a (compilation). Adopted to match Bolatto et al. (2008) where possible.

3. DATA

To carry out this experiment we require maps of IR (to estimate Σ_{dust}), CO, and H I emission. Such maps have been published for M 31, M 33, NGC 6822, the LMC, and the SMC. We refer to the original papers for details of the observations, reduction, and data.

For M 31, we use the CO map taken by Nietten et al. (2006) using the IRAM 30 m telescope. This map has already been masked by Nietten et al. (2006) and so contains only positive signal. We trace H I using the 21 cm map of Brinks & Shane (1984), obtained with the Westerbork Synthesis Radio Telescope (WSRT). Gordon et al. (2006) present *Spitzer* maps at 24, 70, and 160 μm .

For M 33, we take CO data from Rosolowsky et al. (2007), which combine BIMA (Engargiola et al. 2003) and FCRAO data (Heyer et al. 2004). We use the WSRT map by Deul & van der Hulst (1987). We use *Spitzer* data reduced following Gordon et al. (2005) and presented by Verley et al. (2007) and Tabatabaei et al. (2007).

We use the first CO map of the LMC obtained by NANTEN (Fukui et al. 1999), the Australia Telescope Compact Array (ATCA) + Parkes H I map of Kim et al. (1998, 2003), and IR maps from the *Spitzer* SAGE legacy program (Meixner et al. 2006; Bernard et al. 2008).

We also use the NANTEN CO map of the SMC (Mizuno et al. 2001), the ATCA + Parkes H I map by Stanimirovic et al. (1999). The SMC IR maps are a combination of data from the SAGE-SMC legacy program (Gordon et al. 2009; K. D. Gordon et al. 2011, in preparation) and the S3MC survey (Bolatto et al. 2007).

For NGC 6822, we use the IRAM 30 m CO map by Gratier et al. (2010), the SINGS *Spitzer* maps presented by Cannon et al. (2006), and the Very Large Array H I map of de Blok & Walter (2003). Gratier et al. (2010) mapped the CO $J = 2 \rightarrow 1$ line for this galaxy, while the rest of our maps are of CO $J = 1 \rightarrow 0$. We follow Gratier et al. (2010) in assuming a line ratio of 0.7; we phrase all of our results in terms of CO $J = 1 \rightarrow 0$ intensity assuming this ratio. We mask the CO map, keeping only emission above $\sim 3\sigma$ at the original $15''$ resolution.

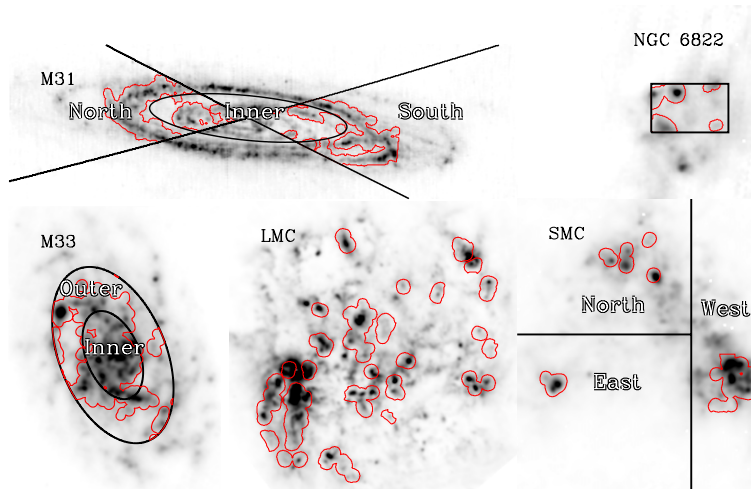


Figure 1. Images of our targets at $160\ \mu\text{m}$ (gray scale) with the region considered enclosed by a red contour. In M 31, M 33, and the SMC, black lines separate regions that we treat separately and labels indicate how we refer to these in the text.

(A color version of this figure is available in the online journal.)

For each galaxy, we convolve all data to the resolution of the coarsest data set and align them on a common astrometric grid. In M 31, M 33, and NGC 6822, we are limited by the resolution of the *Spitzer* $160\ \mu\text{m}$ data and so convolve all data to have a $45''$ (FWHM) Gaussian point-spread function (PSF). In the LMC, the NANTEN CO data limit our resolution to $>2.6''$; because signal to noise in the CO map is also a concern, we convolve all data to $4''$ resolution. The NANTEN CO data also set the resolution in the SMC, where we convolve all data to $2.6''$ resolution.

In the LMC and SMC, we subtract a foreground from the IR maps. Following Bot et al. (2004), we remove a scaled version of the Milky Way H I over these lines of sight (for the exact approach, see Leroy et al. 2009). In M 33 and M 31, the reduction imposes the condition that the intensity is 0 away from the galaxy, making a cirrus subtraction unnecessary. In NGC 6822, Cannon et al. (2006) already removed a Galactic foreground.

The statistical uncertainty in the CO maps is about $0.30\ \text{K km s}^{-1}$ in M 31, $0.35\ \text{K km s}^{-1}$ in M 33, $0.30\ \text{K km s}^{-1}$ in the LMC, $0.01\ \text{K km s}^{-1}$ in NGC 6822, and $0.08\ \text{K km s}^{-1}$ in the SMC (though in each case this varies somewhat with position). The statistical noise in the H I maps is very roughly $1\text{--}3\ M_{\odot}\ \text{pc}^{-2}$ with the uncertainty dominated by imperfect knowledge of the H I opacity and the reconstruction of extended emission. The noise in the IR maps is $\sim 0.2\ \text{MJy sr}^{-1}$ at $70\ \mu\text{m}$ and $\sim 0.7\ \text{MJy sr}^{-1}$ at $160\ \mu\text{m}$. The zero point in the IR maps is uncertain by $\sim 0.1\ \text{MJy sr}^{-1}$ at $70\ \mu\text{m}$ and $\sim 0.5\ \text{MJy sr}^{-1}$ at $160\ \mu\text{m}$.

Throughout this paper, IR intensity has units of MJy sr^{-1} , color-corrected to the *IRAS* scale. H I surface density has units of $M_{\odot}\ \text{pc}^{-2}$ and includes a factor of 1.36 to account for helium. In the SMC and the LMC, H I includes an opacity correction based on Dickey et al. (2000). In M 31, M 33, and NGC 6822, we have assumed that the H I is optically thin. CO $J = 1 \rightarrow 0$ intensity has units of K km s^{-1} and is related to H_2 surface density, in units of $M_{\odot}\ \text{pc}^{-2}$, by a factor α_{CO} that includes helium (so that $\Sigma_{\text{H}_2} = \alpha_{\text{CO}} I_{\text{CO}}$); if $X_{\text{CO}} = 2 \times 10^{20}\ \text{cm}^{-2}\ (\text{K km s}^{-1})^{-1}$ then $\alpha_{\text{CO}} = 4.4\ M_{\odot}\ \text{pc}^{-2}\ (\text{K km s}^{-1})^{-1}$.

4. METHOD

Our goal is to identify regions where both H I and H_2 contribute significantly to the interstellar medium (ISM), use

the IR intensity in these regions to estimate the dust column, and then harness the assumption that gas and dust are linearly related to solve for α_{CO} .

4.1. Sampling and Target Region

This experiment leverages our knowledge of H I column to infer α_{CO} . It thus works best in regions where both H I and H_2 are important to the ISM mass budget. If we target areas where H I dominates then α_{CO} has little or no impact on δ_{GDR} while if we target areas with only H_2 then α_{CO} and δ_{GDR} are degenerate.

For our targets and resolution, being dominated by H_2 is not a concern for any reasonable α_{CO} . On the other hand, each target has large areas where the ISM is overwhelmingly H I. Especially in M 31 and M 33, much of the H I is at large radius and appears to have a different δ_{GDR} from the inner galaxy (Nieten et al. 2006). We mostly avoid these H I-only regions, instead targeting the part of each galaxy near where CO is detected. This gives us a range of total gas surface densities and relative contributions by H_2 and H I, allowing us to constrain α_{CO} and δ_{GDR} .

We define our target region by a $\approx 3\sigma$ intensity cut in the convolved CO map, $I_{\text{CO}} \geq 1\ \text{K km s}^{-1}$ in M 31, M 33, and the LMC, $I_{\text{CO}} \geq 0.25\ \text{K km s}^{-1}$ in the SMC, and $I_{\text{CO}} \geq 0.03\ \text{K km s}^{-1}$ in NGC 6822. We reject small regions (area \lesssim a resolution element) as likely noise spikes and then consider all area within about one resolution element of the remaining emission. Finally, we require a line of sight to have significant IR emission to be included; this is $I_{160} \geq 5\ \text{MJy sr}^{-1}$ in NGC 6822, $I_{160} \geq 10\ \text{MJy sr}^{-1}$ in all other targets. The result resembles loosely circling bright CO emission by hand. Figure 1 shows the target regions in contour on top of the $160\ \mu\text{m}$ map.

In M 31, M 33, and the SMC treating the whole galaxy at once causes problems with our model, which assumes a constant α_{CO} and δ_{GDR} across the area studied. Previous work arrived at similar conclusions. Nieten et al. (2006) observed δ_{GDR} to be higher in the inner part of M 31 than the 10 kpc ring containing most of the CO. In M 33, bright CO extends a fair distance out into the disk, but based on radial profiles of H I, CO, and $160\ \mu\text{m}$ intensity it is immediately clear that this galaxy, too, has a strong radial gradient in δ_{GDR} . The SMC's CO emission is clustered into three distinct regions that show evidence for local variations in their δ_{GDR} , α_{CO} , and GMC properties (Leroy et al. 2007; Muller et al. 2010).

Table 2
Dust-based α_{CO} for Local Group Galaxies

System	$\alpha_{\text{CO}}^{\text{a}}$	Uncertainty ^b				Correlation ^c	Scatter ^d ($\log_{10} \delta_{\text{GDR}}$)	Notes
		Stat.	Rob.	Assump.	Tot.			
M 31								
Inner	2.1	0.14	0.03	0.26	0.29	0.68 ± 0.02	0.21	U unconstrained
South	10.0	0.05	0.01	0.12	0.13	0.85 ± 0.02	0.11	U unconstrained
North	4.2	0.05	0.02	0.19	0.20	0.83 ± 0.02	0.15	U unconstrained
M 33								
Inner	8.4	0.07	0.03	0.15	0.17	0.76 ± 0.03	0.08	
Outer	5.0	0.09	0.05	0.17	0.20	0.76 ± 0.03	0.10	
LMC	6.6	0.04	0.02	0.14	0.14	0.84 ± 0.01	0.14	
NGC 6822	24	0.13	0.13	0.26	0.31	0.56 ± 0.07	0.18	Averaged colors
SMC								
West	67	0.06	0.02	0.08	0.10	0.91 ± 0.04	0.09	Subtracted $\Sigma_{\text{H I}} = 40 M_{\odot} \text{ pc}^{-2\text{e}}$
East	53	0.08	0.04	0.44	0.45	0.95 ± 0.11	0.07	Subtracted $\Sigma_{\text{H I}} = 60 M_{\odot} \text{ pc}^{-2\text{e}}$
North	85	0.16	0.05	0.11	0.20	0.47 ± 0.06	0.15	Subtracted $\Sigma_{\text{H I}} = 20 M_{\odot} \text{ pc}^{-2\text{e}}$

Notes.

^a Best fit. Units of $M_{\odot} \text{ pc}^{-2} (\text{K km s}^{-1})^{-1}$ including helium.

^b Estimated 1σ uncertainty in $\log_{10} \alpha_{\text{CO}}$ for each source of uncertainty. “Stat.”—statistical (from Monte Carlo); “Rob.”—robustness to removal of data (from bootstrapping); “Assump.”—variation of assumptions.

^c Linear correlation coefficient relating Σ_{gas} and Σ_{dust} for best-fit α_{CO} . Uncertainty gives 1σ scatter for random re-pairings of data.

^d 1σ scatter in $\log_{10} \delta_{\text{GDR}}$ in dex for best-fit α_{CO} .

^e Based on the fit of $\Sigma_{\text{H I}}$ to Σ_{dust} at low Σ_{dust} .

To isolate regions with fixed α_{CO} and δ_{GDR} , we separate each galaxy into several zones. We treat the “inner” part of M 31 separately from the 10 kpc ring and further divide the ring into a “north” and “south” part. We exclude 60° around the minor axis (in the plane of the galaxy) of M 31 (see Section 4.3). We break M 33 into an “inner” zone where $r_{\text{gal}} < 2$ kpc and an “outer” zone where $2 \text{ kpc} < r_{\text{gal}} < 4$ kpc. We divide the SMC into three parts: a “west” region, a “north” region, and an “east” region. Our regions in the SMC deliberately exclude two clouds near the center of the galaxy identified in Leroy et al. (2007) to have high CO-to-IR ratios; including these clouds leads to even worse solutions for this part of the SMC. Black lines and labels in Figure 1 indicate the divisions for each galaxy.

After the target regions are defined, we sample each map using a hexagonal grid spaced by $1/2$ the resolution (i.e., $22''.5$ in M 31, $20''$ in M 33, $2''$ in the LMC, $22''.5$ in NGC 6822, and $1/3$ in the SMC). This yields a matched, approximately Nyquist-sampled set of measurements of I_{70} , I_{160} , I_{CO} , and $\Sigma_{\text{H I}}$.

4.2. Estimating Dust Along the Line of Sight

We follow the approach of Draine & Li (2007) and Draine et al. (2007) to estimate the amount of dust along the line of sight. These papers present models that can be used to estimate the dust mass and incident radiation field from IR intensities. Following Draine et al. (2007) and Muñoz-Mateos et al. (2009), we search a grid of models illuminated by different radiation fields to find the best-fit dust mass surface density, Σ_{dust} , for each set of IR intensities. A slight difference between our fits and those papers is that we quote the geometric mean of the dust mass across the region of parameter space where $\chi^2 < \chi_{\text{min}}^2 + 1$ (i.e., within 1 of the χ^2 for the best-fit model). We present the results of our own direct grid-search fits, but during analysis made extensive use of the work of Muñoz-Mateos et al. (2009), who parameterized the results of model fitting over a wide range of parameter space have been as functions of the IR intensity at 24, 70, and 160 μm .

We only need a linear tracer of dust mass to solve for α_{CO} , the normalization affects δ_{GDR} but not α_{CO} . While values of δ_{GDR} that we find are interesting on their own, the overall normalization of the Draine & Li (2007) models do not affect our results for α_{CO} . Before settling on the Draine & Li (2007) models, we also used modified blackbody fits with a range of emissivities to estimate the dust opacity, τ_{160} . We obtained very similar results for α_{CO} using that approach, in the end preferring the Draine & Li (2007) models mainly for their more straightforward handling of the 70 μm band, which can include significant out-of-equilibrium emission. When we derive the uncertainties associated with our assumptions (Section 4.4 and Appendix B), we adopt either a modified blackbody or the Draine & Li (2007) models with equal probability. When using a modified blackbody fit, we include a variable fraction of 70 μm emission from an out-of-equilibrium population and emissivity power-law index in the calculation.

M 31. M 31 is quiescent compared to our other targets. It has a very low I_{70}/I_{160} , implying very low radiation fields or colder dust temperatures (Gordon et al. 2006). Montalto et al. (2009) showed that with only *Spitzer* data the radiation field illuminating the dust is unconstrained. In addition to poor constraints on the model, these low I_{70}/I_{160} make ratio maps extremely sensitive to artifacts or contamination by point sources. M 31, of all our targets, will benefit most from the additional spectral energy distribution (SED) coverage offered by *Herschel*. Our approach in the meantime is to treat all points in M 31 with as though they had the median IR color across the whole galaxy. We implement the recommendation by Draine et al. (2007) that in the absence of submillimeter data, the radiation field be limited to 0.7 times the local value. This treatment effectively assumes that value everywhere in M 31 and uses the $I_{160} \mu\text{m}$ to estimate the dust mass. We note this uncertainty in Table 2.

NGC 6822. NGC 6822 shows the faintest IR emission of any of our targets. As a result, many of the variations in I_{70}/I_{160} appear driven by noise and artifacts rather than T_{dust} variations. Gratier et al. (2010) noted the difficulty of deriving

dust temperatures for each line of sight. Based on plots of I_{70} versus I_{160} , we identify two main “colors” in our data. We assign each line of sight the median color for its group, with the cut at $I_{70}/I_{160} = 0.6$. We note this uncertainty in Table 2.

4.3. Diffuse H I

Gas with different δ_{GDR} may be superposed along the line of sight, in which case our assumption of a single δ_{GDR} no longer applies. In some cases, we expect there to be a diffuse H I component with little or no associated dust along the line of sight. Such a component requires that we introduce an additional term into Equation (2) so that Σ_{gas} remains finite once $\Sigma_{\text{dust}} \sim 0$.

The simplest example of this is an edge-on spiral galaxy with a strong radial gradient in δ_{GDR} . M 31 is inclined and does show a gradient in δ_{GDR} (Nieten et al. 2006). The pile-up of many different radii along a single line of sight will be most severe along the minor axis and Equation (2) does not appear to describe these data as well as those along the major axis. Because we have plenty of data, we simply exclude 60° around the minor axes from our analysis. This improves the stability of our solution. No other correction appears necessary.

The SMC has an extended distribution of H I that may also be very elongated along the line of sight. In this H I envelope and away from the main star-forming regions (in the “Wing” and “Tail”), δ_{GDR} is observed to be high (Bot et al. 2004; Leroy et al. 2007; Gordon et al. 2009). Similar results are found for other dwarf irregulars (Walter et al. 2007; Draine et al. 2007). Given the very high column densities found in the SMC, it is plausible that low δ_{GDR} H I lies along the line of sight.

To account for an envelope of dust-poor H I, we subtract a diffuse component from the SMC H I map before fitting for α_{CO} . We estimate this component via an ordinary least squares bisector fit relating Σ_{dust} and $\Sigma_{\text{H I}}$ at low Σ_{dust} , where H I is likely to represent most of the gas. This line implies a value of $\Sigma_{\text{H I}}$ where $\Sigma_{\text{dust}} = 0$, which we take as our estimate of the diffuse H I. We estimate a diffuse component of $\Sigma_{\text{H I}} = 40, 20$, and $60 M_\odot \text{pc}^{-2}$ for the western, northern, and eastern parts of the SMC. Similar fits to the other targets suggest a diffuse H I component with magnitude below $10 M_\odot \text{pc}^{-2}$, usually consistent with zero. Our uncertainty estimates include a 20% (1σ) uncertainty on this diffuse component in the SMC and $\pm 5 M_\odot \text{pc}^{-2}$ in the case of galaxies other than the SMC.

This subtraction of diffuse H I differs from Leroy et al. (2007, 2009, though the latter applied this approach in some of the analysis). The effect on α_{CO} is largest in the “east” section of the SMC, which is embedded in the mostly diffuse Wing.

4.4. Solution

Appendices A and B lay out our method of solution and uncertainty estimates in detail. We identify the best-fit α_{CO} for each data set as the value that minimizes the point-to-point (rms) scatter in $\log_{10} \delta_{\text{GDR}}$. We estimate the uncertainty from three sources: (1) statistical noise, (2) robustness to removal of individual data, and (3) assumptions. These are reported in Table 2 and we take the overall uncertainty to be the sum of all three terms in quadrature.

4.5. Limitations of the Model

Our model has several important limitations. It cannot recover a pervasive, CO-free H_2 component like that suggested for the LMC by Bernard et al. (2008). To derive such a component, we would need to make strong assumptions about δ_{GDR} . We

derive α_{CO} for H_2 associated with CO emission on $\sim 100 \text{ pc}$ scales, essentially α_{CO} for GMCs and their envelopes. Based on UV spectroscopy (e.g., Tumlinson et al. 2002), we consider a pervasive H_2 phase unlikely, but our experiment makes no test of this idea one way or the other.

We assume that δ_{GDR} does not vary between the atomic and molecular ISM. In fact, observations and theory suggest the δ_{GDR} does correlate with density. The depletion of heavy elements from the gas phase increases with increasing density (Jenkins 2009), though absorption measurements cannot probe to very high densities. Meanwhile, accounting for the observed dust abundance appears to require buildup of dust in molecular clouds (Dwek 1998; Zhukovska et al. 2008; Draine 2009). A lower δ_{GDR} in dense, molecular gas directly, linearly scales our derived α_{CO} . Dust already accounts for $\sim 50\%$ of the relevant heavy elements, so this effect cannot exceed a factor of ~ 2 in magnitude. In fact, the effect should be even less severe because we already study mainly the peaks of the gas distribution, where we expect H I to also have high densities.

Our dust modeling also implicitly assumes that the dust emissivity does not vary between the atomic and molecular gas. Observations suggest that dust properties do change between the diffuse and dense ISM, with an enhanced emissivity in dense gas. The best evidence for this comes from a $\sim 30\%$ – 50% increase in far-IR optical depth relative to optical extinction at high columns ($\sim 1 \text{ mag}$; e.g., Arce & Goodman 1999; Dutra et al. 2003; Cambr sy et al. 2005). Direct comparison of virial masses to submillimeter emission suggests a similar enhancement (Bot et al. 2007). The origin of this enhanced emissivity is thought to be a change in the size distribution of dust, with “fluffy,” low-albedo grains created in dense environments (Dwek 1997; Stepnik et al. 2003; Cambr sy et al. 2005). As with δ_{GDR} variations, emissivity variations directly scale the derived α_{CO} .

Our best estimate is that emissivity and δ_{GDR} variations bias our measured α_{CO} high by a factor of ~ 1.5 – 2.0 . Because this estimate distills a variety of literature results, none of them definitive, applying such a correction after the fact would simply confuse our results. More importantly, we have no handle on how these factors vary with environment, though we expect weaker effects at low metallicity, where shielding is weaker. We highlight a quantitative understanding of δ_{GDR} and dust emissivity vary with environment as the most important systematics that must be addressed to improve dust-based derivations of α_{CO} .

Finally, our data cannot rule out a pervasive population of very cold dust. We consider this unlikely and neglect it throughout the paper (e.g., see Draine et al. 2007). If such a population exists, the *Herschel Space Observatory* will identify it and our picture of dust will change dramatically over the next few years. However, we note that preliminary results suggest that dust masses are not dramatically affected by the inclusion of *Herschel* data (Gordon et al. 2010). Other systematics in using dust to trace H_2 have been discussed at length elsewhere (Israel 1997a, 1997b; Schnee et al. 2005; Leroy et al. 2007, with references to many other works therein) and we do not repeat them here. Our best estimate is that none of these represent a major concern. Almost all will be addressed by the inclusion of long-wavelength *Herschel* data (and are already improved relative to *IRAS* by using *Spitzer*’s $160 \mu\text{m}$ band).

5. RESULTS

Figure 2 plots scatter in $\log_{10} \delta_{\text{GDR}}$ as a function of α_{CO} for our targets. In the background, a normalized histogram

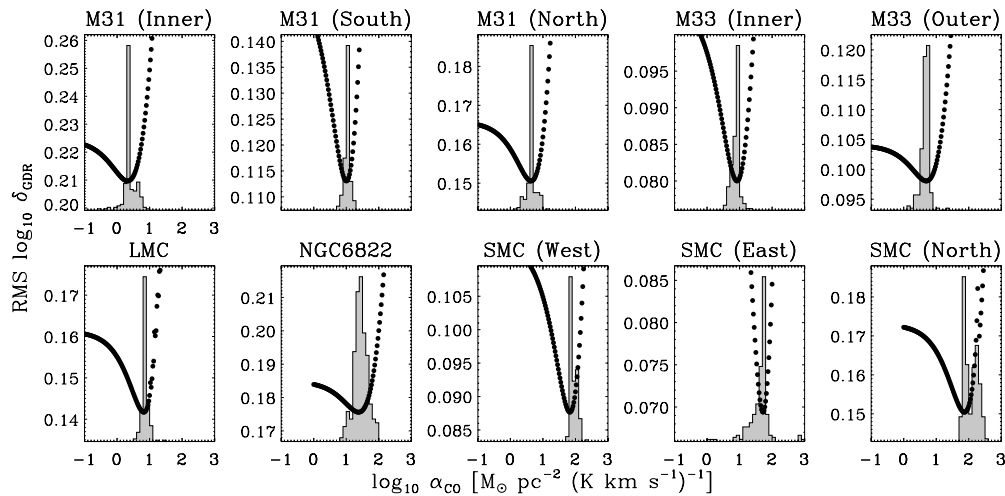


Figure 2. Scatter in $\log_{10} \delta_{\text{GDR}}$ as a function of α_{CO} ; each dot shows a calculation for a trial α_{CO} . The shaded histograms in the background show the distribution of best-fit α_{CO} achieved across bootstrapping and variation of assumptions; they give some indication of the likelihood of a given α_{CO} describing the data.

indicates the distribution of best-fit α_{CO} derived across the uncertainty exercises nos. 2 (bootstrapping) and 3 (variation of assumptions). We find clear minima in each data set, which we report in Table 2 with associated uncertainties. We also quote the linear correlation coefficient between gas and dust and the scatter in $\log_{10} \delta_{\text{GDR}}$ for the best-fit α_{CO} . Both quantities indicate the degree to which our model describes the system.

The scatter plots in Figures 3–5 show gas (y-axis) as a function of dust (x-axis) for each target. In the left column, Σ_{gas} is calculated from H I alone, the middle column shows $\Sigma_{\text{gas}} = \alpha_{\text{CO}} I_{\text{CO}}$ for our best-fit α_{CO} , and the right column shows total gas ($\Sigma_{\text{gas}} = \Sigma_{\text{H I}} + \alpha_{\text{CO}} I_{\text{CO}}$). In each case, the last column is a better match to a line through the origin (i.e., a single δ_{GDR}) than the first two.

The southern part of M 31 exemplifies the signal that we look for. H I correlates well with dust at low Σ_{dust} . At the high end, Σ_{dust} increases without a corresponding increase in H I (left panel). CO correlates well with Σ_{dust} at high Σ_{dust} but drops to low values (or zero) while there is still significant dust, so that the x-intercept of the CO– Σ_{dust} relationship is not zero (middle panel). The gas becomes mostly molecular above a certain Σ_{dust} and is mostly atomic below this. Our best α_{CO} stitches these regimes together, allowing a single δ_{GDR} to span all data.

5.1. Comments on Solutions

Before arriving at these results, we varied our methodology significantly. We tried different dust treatments, methods of solution, sampling regions, and treatments of diffuse H I. Most variations yield similar results to what we present here but a few cases are worth comment.

First, the northern part of the SMC is not well described by our model even after we excluded the high CO-to-IR clouds. Several distinct groups of data appear in the scatter plots for this region, suggesting local variations in δ_{GDR} or α_{CO} . The data for this region are already good (Muller et al. 2010), so improved modeling—multiple dust and H I components, local variations in α_{CO} and δ_{GDR} —seems like the most acute need. In the meantime, our solution minimizes δ_{GDR} and yields a result consistent with the other SMC regions.

NGC 6822 yields reasonable solutions but is somewhat unstable to the choice of methodology. Adjusting the dust treatment, background subtraction, or weighting can change the

best-fit α_{CO} by $\sim 50\%$. This instability results mostly from the low signal-to-noise ratio and dynamic range in the data. These, in turn, are low because of the large distance of NGC 6822 compared to the SMC or the LMC, which makes observations challenging. The resulting low intensities also make confusion with the Milky Way an issue (Cannon et al. 2006). Improved resolution from *Herschel* or ALMA should allow a greater range of Σ_{dust} as individual clouds are resolved. This will enable a stronger constraints on α_{CO} .

The inner part of M 31 is also somewhat unstable to the choice of methodology—especially region definition and fitting method. Best-fit solutions can range from $\alpha_{\text{CO}} \sim 1$ to 5. The most likely cause is variations in δ_{GDR} and α_{CO} within the region studied—the data do not appear to be a plane in CO–H I–dust space. Both improved modeling and better IR SED coverage will help this case.

We emphasize that our approach to the SMC is conservative. We subtract a diffuse H I foreground, correct for high optical depth H I, and solve for δ_{GDR} in the star-forming regions only—rendering us insensitive to any pervasive CO-free H_2 component. All of these choices lower α_{CO} , bringing it closer to the other galaxies, but the SMC still exhibits notably high α_{CO} . The more straightforward approaches employed in Israel (1997a), Leroy et al. (2007), and Leroy et al. (2009) yield even higher α_{CO} .

5.2. α_{CO} versus Metallicity

Figure 6 shows α_{CO} (left) and δ_{GDR} (right) as a function of metallicity. Table 2 gives the adopted metallicity for each target, which unfortunately represent a major source of uncertainty. Literature values span several tenths of a dex for most of our systems and internal variations in $12 + \log(\text{O}/\text{H})$ often exist even where strong gradients are absent. We show a 0.2 dex uncertainty in $12 + \log(\text{O}/\text{H})$ in our plots to reflect this uncertainty.

Figure 6 shows that δ_{GDR} is a clear function of metallicity, increasing with decreasing metallicity. This clear, one-to-one dependence of δ_{GDR} on metallicity provides a consistency check on our solutions for α_{CO} . The data are roughly consistent with a linear relation (i.e., a fixed fraction of metals in dust), though a fit yields a slightly sublinear slope, $\log_{10} \delta_{\text{GDR}} = (9.4 \pm 1.1) - (0.85 \pm 0.13) [12 + \log(\text{O}/\text{H})]$. Our focus on star-forming regions likely biases us toward high δ_{GDR} ; studies of

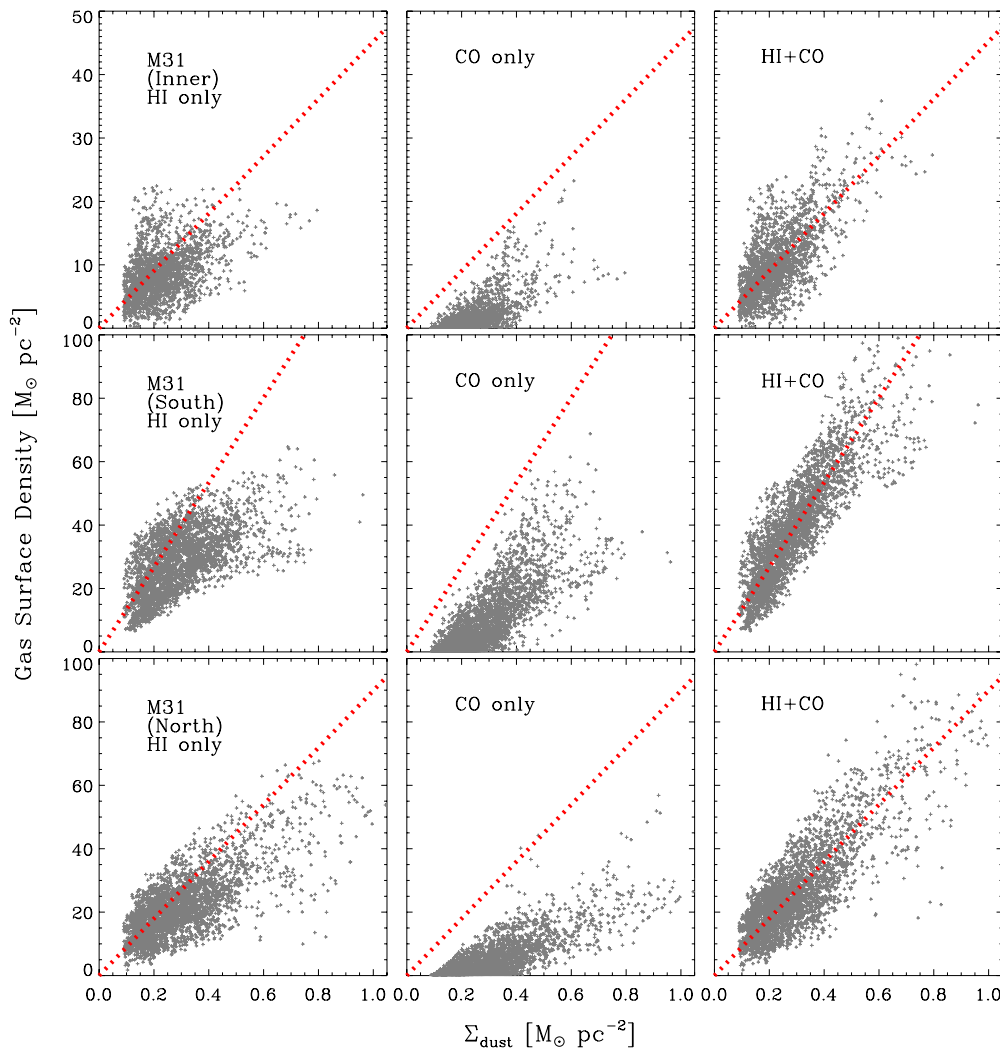


Figure 3. Scatter plots showing Σ_{gas} as a function of Σ_{dust} for M 31. The columns show the relationship between dust (x-axis) and (left) H I, (middle) H₂ derived from CO using our best-fit α_{CO} , and (right) total (H I + H₂) gas. Our best-fit α_{CO} yields reasonable linear scalings between total gas and dust in each system (the red line shows the median δ_{GDR}), usually a clear improvement on the relationship between dust and either phase alone.

(A color version of this figure is available in the online journal.)

all material find a steeper relation (Lisenfeld & Ferrara 1998; Muñoz-Mateos et al. 2009).

In the left panel of Figure 6, we plot the best-fit α_{CO} as a function metallicity. A gray area shows the commonly accepted range of values for the Milky Way (Bloemen et al. 1986; Solomon et al. 1987; Strong & Mattox 1996; Dame et al. 2001; Heyer et al. 2009). A dashed line shows the α_{CO} argued by Draine et al. (2007) to offer the best consistency between dust and gas measurements in SINGS galaxies. The molecular ring in M 31, both parts of M 33, and the LMC span a factor of ~ 2 – 3 in metallicity but show little clear gradient in α_{CO} . All three appear broadly consistent with the Milky Way. We find higher α_{CO} in NGC 6822 and the SMC, but the rise relative to the higher metallicity systems much steeper than linear. Figure 6 therefore suggests a jump from “normal” to “high” α_{CO} at metallicity $\sim 1/4$ the solar value rather than a steady dependence of α_{CO} on metallicity. At the high-metallicity end, the inner part of M 31 does suggest a low α_{CO} . It is unclear how much weight to ascribe to this point and whether the low α_{CO} is primarily a product of metallicity: the solution is somewhat unstable and a number of other conditions differ between the bulge of M 31 and our other targets. However, the point does highlight that

lower-than-Galactic α_{CO} has often been observed, especially in extreme, dust-rich systems (e.g., Downes & Solomon 1998).

6. DISCUSSION

First, we emphasize a very basic result: combining H I, CO, and IR emission we obtain reasonable solutions for α_{CO} across the Local Group. In M 31, M 33, and the LMC α_{CO} appears consistent, within the uncertainties, with the Milky Way. In most targets, our α_{CO} agree well with previous determinations using other methods. Despite its simplicity and the potential importance of systematic effects, the approach outlined here produces consistent results. A lack of quantitative constraints on how the emissivity and δ_{GDR} change between the atomic and molecular ISM (ideally measured at several metallicities) remains the most significant obstacle to derive robust absolute values of α_{CO} from this approach. We cite circumstantial evidence that these effects combined may cause us to overestimate α_{CO} everywhere by a factor of ~ 1.5 – 2 but emphasize the need for better constraints to improve the precision of this approach. In the meantime we have, we believe, an internally robust measurement of α_{CO} spanning an order of magnitude in metallicity.

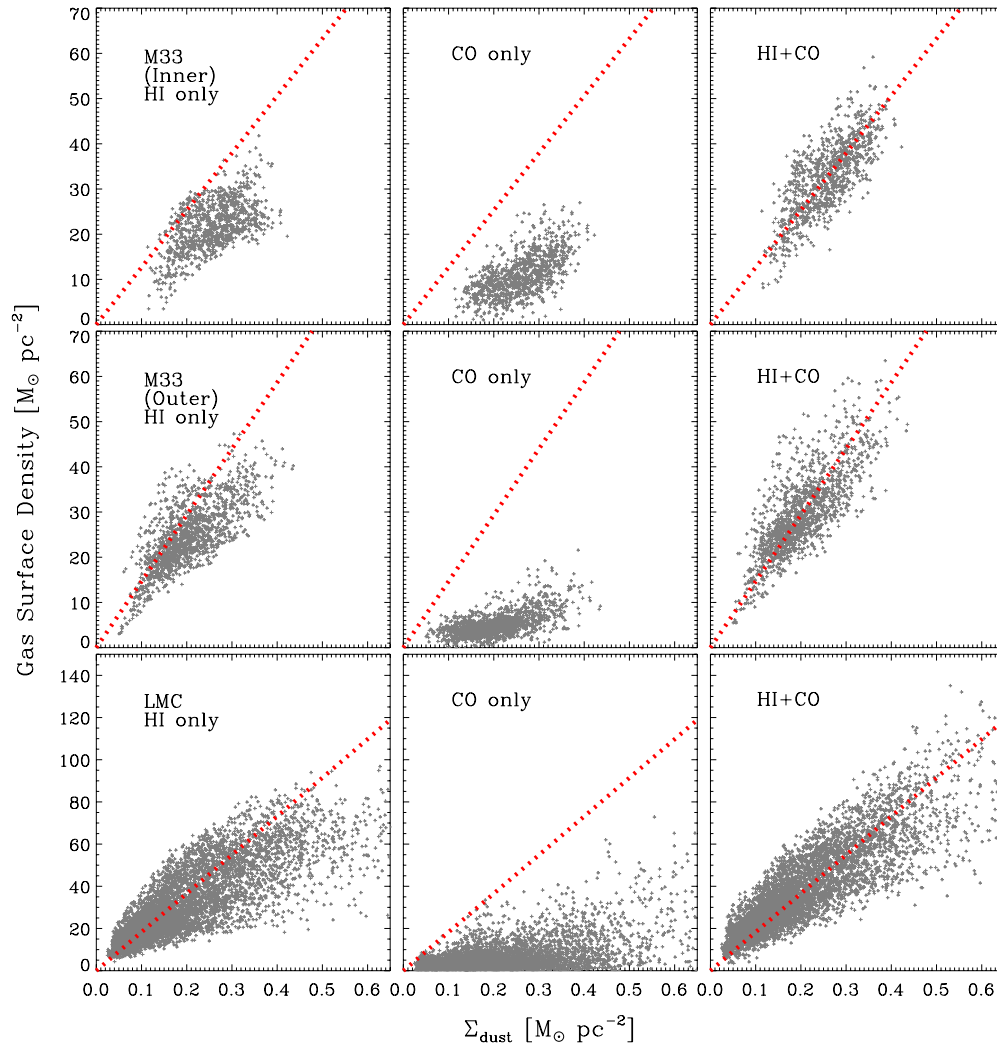


Figure 4. Same as Figure 3 for M33 and the LMC.

(A color version of this figure is available in the online journal.)

6.1. CO-dark Gas at Low Metallicities

Does a rapid increase in α_{CO} over a narrow range in metallicity make physical sense? The metallicity dependence of α_{CO} is likely driven by “CO-dark” H_2 at low extinctions. In regions with low metallicity, a significant mass of H_2 is found in the outer parts of clouds where the carbon is mostly C^+ rather than CO (e.g., Maloney & Black 1988; Israel 1997b; Bolatto et al. 1999). Both Glover & Mac Low (2010) and Wolfire et al. (2010) recently studied this problem by modeling molecular clouds. They find that the dust extinction is the key parameter determining the fraction of CO-dark gas or α_{CO} . For clouds with mean extinction $A_V \sim 8$ mag, such as those in the Milky Way, Wolfire et al. (2010) find a fraction of CO-dark gas $f_{\text{DG}} \sim 30\%$, in rough agreement with several observations of nearby clouds (Grenier et al. 2005; Abdo et al. 2010). At intermediate metallicities, the CO-dark H_2 is not dominant, so that even a significant fractional change does not impact α_{CO} very much. For example, in the calculations by Wolfire et al. (2010) going from the metallicity of M 31 to that of the LMC causes a doubling of the CO-dark gas fraction, from $f_{\text{DG}} \approx 20\%$ to $f_{\text{DG}} \approx 40\%$, but the corresponding effect on α_{CO} is only a factor of ~ 1.3 , easily within the uncertainties of our study. As the mean extinction through the cloud decreases

due to the effects of metallicity on the gas-to-dust ratio the increase in the fraction of CO-dark H_2 makes it the dominant molecular component, at which point α_{CO} is very rapidly driven upward.

Our measurements suggest that CO-dark gas becomes an important component in the metallicity range $12 + \log(\text{O}/\text{H}) \sim 8.2\text{--}8.4$. With such a small sample, we cannot be sure that this is a general result, but it is in good agreement with the expectation from Wolfire et al. (2010). Above these metallicities, variations in the fraction of CO-dark gas will still exist, but their influence on the value of α_{CO} will be small. Excitation of the molecular gas (particularly due to temperature variations) will be likely the dominant factor setting α_{CO} in molecule-rich systems. This is probably the cause of the low α_{CO} observed in LIRGs and ULIRGs (e.g., Downes & Solomon 1998), which have solar or slightly subsolar metallicities (e.g., Rupke et al. 2008). Within galaxies, the radiation field incident on the molecular gas may also play a role, a fact emphasized by Israel (1997a). Unfortunately, the size scales involved make this extragalactic measurement difficult. While Israel (1997a) found strong quantitative support for the influence of the radiation field on α_{CO} , Pineda et al. (2009) and Hughes et al. (2010) recently failed to detect this effect in carefully controlled experiments in the LMC.

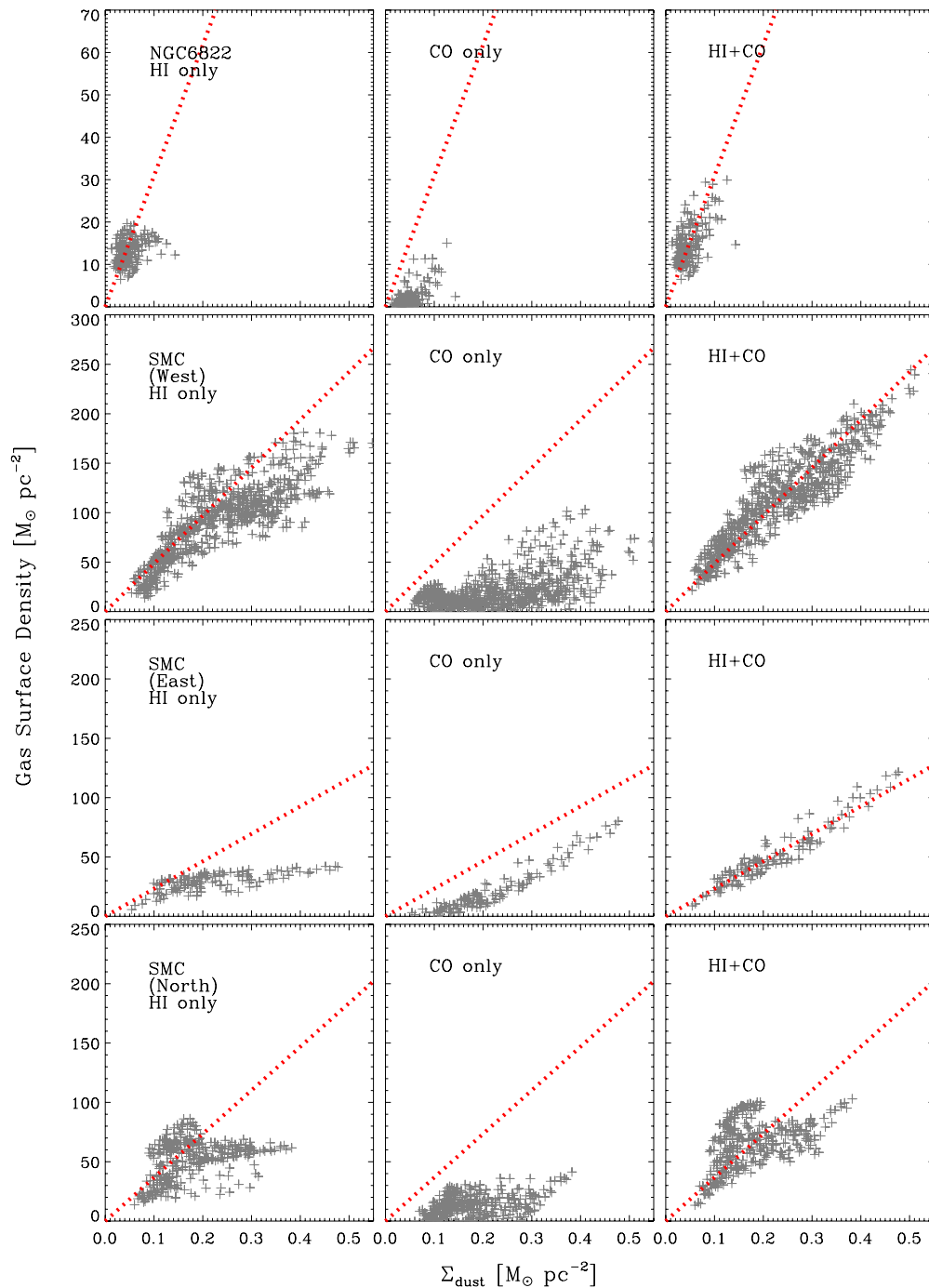


Figure 5. Same as Figure 3 for NGC 6822 and the SMC.

(A color version of this figure is available in the online journal.)

6.2. Comparison with the Literature

Many authors have measured α_{CO} using a variety of techniques. We will not attempt to summarize the literature, but focus on comparisons to two sets of measurements: (1) previous applications of IR-based techniques and (2) high spatial resolution measurements of dynamical masses using CO emission.

We measure high α_{CO} in the SMC and NGC 6822. This agrees with a larger trend in which IR photometry and spectroscopy suggest high α_{CO} in the range $12 + \log(\text{O}/\text{H}) \lesssim 8.0\text{--}8.2$. Israel (1997a) saw this in a number of irregulars. Rubio et al. (2004), Leroy et al. (2007), and Leroy et al. (2009) found similar results

in the SMC, though as we note in Section 5.1 we actually solve for a somewhat lower α_{CO} than these studies—a fact we attribute to our focus on deriving δ_{GDR} from the H I immediate associated with the star-forming region. Gratier et al. (2010) found the same high α_{CO} for NGC 6822 using several approaches. Using far-infrared spectroscopy, Madden et al. (1997) found indications of high α_{CO} in IC 10, a Local Group galaxy with metallicity similar to NGC 6822 (we do not include IC 10 in this study because it lies near the Galactic plane and has considerable IR foregrounds). Pak et al. (1998) reached similar conclusions in the SMC. Dust continuum modeling by Bernard et al. (2008) and Roman-Duval et al. (2010) found a mixed picture in the LMC, also consistent with our findings. Note that in contrast

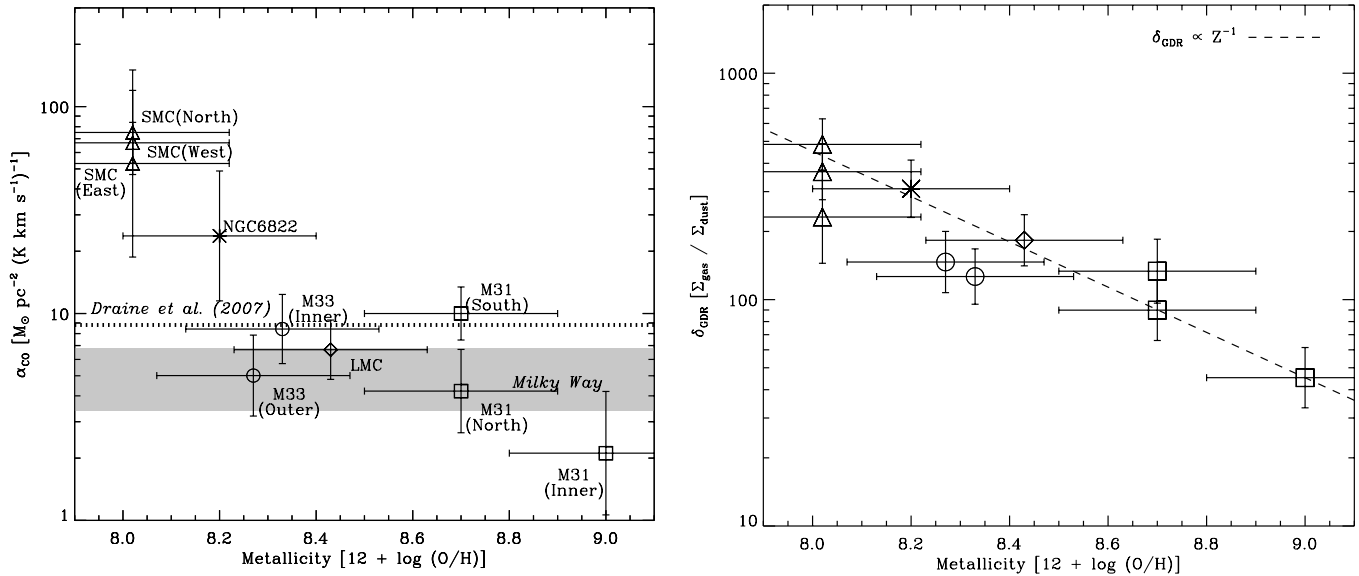


Figure 6. Left: α_{CO} as a function of metallicity. The gray region shows the range of commonly used α_{CO} for the Milky Way and the dashed line indicates the value argued for by Draine et al. (2007) studying integrated photometry of SINGS galaxies. Right: the gas-to-dust ratio δ_{GDR} as a function of the same metallicities. The dashed line indicates a linear scaling.

with this broad agreement, recent work on diffuse lines of sight in the Milky Way (Liszt et al. 2010) suggests that the ratio of CO brightness to H₂ column density is not a strong function of column density.

Figure 7 compares α_{CO} as a function of metallicity between this study and the literature. The points in red indicate IR-based measurements. In detail, our measurements (circles) yield *lower* α_{CO} than previous IR-based studies. We suspect that this is mainly because we solve for α_{CO} without assuming δ_{GDR} or measuring it far away from the region of interest. One likely sense of systematic variations in δ_{GDR} is that δ_{GDR} is likely to be higher in the dense gas close to molecular complexes, which tend to reside mainly in the stellar disk, than in a diffuse, extended H I disk (e.g., Stanimirovic et al. 1999; Draine et al. 2007; Muñoz-Mateos et al. 2009). If δ_{GDR} is taken to be too high, Equation (2) yields a corresponding overestimate of α_{CO} . In the SMC, our attempt to remove a diffuse H I component along the line of sight also leads to lower α_{CO} (Section 5.1), though it is less clear that our approach is correct in that case. Regardless of the cause, by simultaneously solving for α_{CO} and δ_{GDR} in the regions of interest in a uniform way across a heterogeneous sample we improve on literature studies of individual galaxies.

A long standing discrepancy exists between IR-based results and high-resolution virial mass measurements based on CO observations. Using virial masses, Wilson (1995), Rosolowsky et al. (2003), and Bolatto et al. (2008) all found weak or absent trends in X_{CO} as a function of metallicity. The blue points in Figure 7 show virial mass results from CO observations with resolution better than 30 pc. The two approaches agree up to about the metallicity of M 33 or the LMC, and then strongly diverge in the SMC. This divergence is most easily understood if the additional H₂ traced by IR lies in an extended envelope outside the main CO-emitting region (Bolatto et al. 2008). Such an envelope can reconcile the virial mass and dust measurements and naturally explains the scale dependence of α_{CO} observed by Rubio et al. (1993) in the SMC. These envelopes could perhaps still have an effect on the velocity dispersion of the material inside it (and consequently the measured virial mass) via surface pressure. Structures with virial parameters $\alpha \leq 1$, however,

are often observed inside local molecular clouds, suggesting that at least in some instances the velocity dispersion does not appreciably show the impact of the surrounding material. An alternative view is argued by Bot et al. (2007, 2010), who observed discrepancies between dust-based masses and virial masses even at fairly small scales. They suggest that magnetic support becomes very strong at low metallicities, perhaps because of higher ionization fractions inside clouds.

7. SUMMARY

We combine CO, H I, and IR measurements to solve for the CO-to-H₂ conversion factor, α_{CO} , in M 33, M 31, NGC 6822, the LMC, and the SMC. We estimate the dust mass from IR intensities and then identify the α_{CO} that produces the best linear relation between total (H I + H₂) gas and dust. We accomplish this finding the α_{CO} and δ_{GDR} that minimize the scatter about Equation (2). We find that α_{CO} is approximately constant (within a factor of two) in M 31, M 33, and the LMC, with a value $\alpha_{\text{CO}} \approx 6 M_{\odot} \text{ pc}^{-2} (\text{K km s}^{-1})^{-1}$. By contrast NGC 6822 and the SMC, the lowest metallicity galaxies in the sample show a drastically higher α_{CO} , ~ 30 and 70 . The resulting gas-to-dust ratio, δ_{GDR} , scales approximately linear with metallicity.

We attribute the behavior of α_{CO} to the transition from the regime where most H₂ is bright in CO to a regime where CO is mostly photodissociated and the bulk of the molecular reservoir is CO-dark. In our sample, this transition occurs around $12 + \log(\text{O}/\text{H}) \sim 8.4$ – 8.2 . With only a limited number of systems, an actual numerical prescription for α_{CO} is beyond the scope of the paper. These results agree qualitatively with a large body of existing work using IR-based techniques, though quantitatively we find lower α_{CO} than previous work (e.g., Israel 1997a), probably because we restrict our analysis to CO-emitting regions.

We thank the anonymous referee for a constructive report and helpful suggestions. We gratefully acknowledge Elias Brinks, John Cannon, and Fabian Walter for sharing their data on M 31 and NGC 6822. We also thank Julia Roman-Duval, Michele

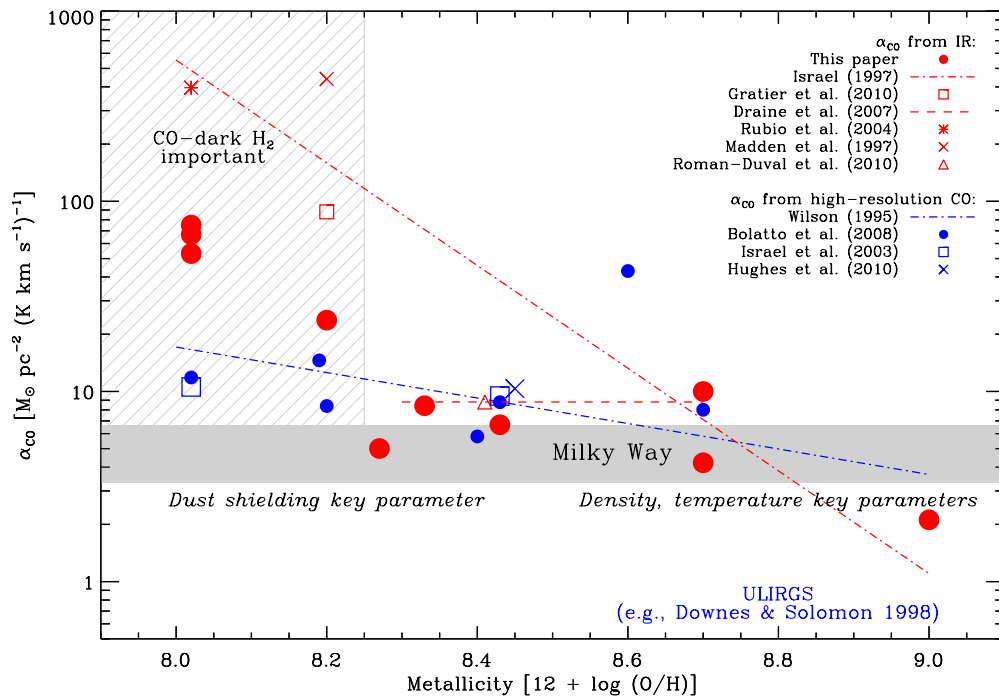


Figure 7. α_{CO} as a function of metallicity. Blue measurements show α_{CO} from virial mass calculations using high-resolution ($\lesssim 30$ pc FWHM) CO mapping. Red measurements show α_{CO} from infrared observations. The “ULIRGs” label indicates roughly the region of parameter space occupied by the dense, excited gas in merger-induced starbursts (Downes & Solomon 1998).

Thornley, Jack Gallimore, Brian Kent, and Erik Mueller for helpful discussions and comments on drafts. We acknowledge the use of NASA’s Astrophysics Data System Bibliographic Services and the NASA/IPAC Extragalactic Database (NED). Support for A.K.L. was provided by NASA through Hubble Fellowship grant HST-HF-51258.01-A awarded by the Space Telescope Science Institute, which is operated by the Association of Universities for Research in Astronomy, Inc., for NASA, under contract NAS 5-26555. A.B. acknowledges partial support from *Spitzer* JPL grant contract 1314022, and from NSF AST-0838178 and NSF-AST0955836.

APPENDIX A

METHOD OF SOLUTION

For a given α_{CO} , we can compute the total gas surface density ($\Sigma_{\text{gas}} = \Sigma_{\text{H}_2} + \Sigma_{\text{H I}}$) for each line of sight. With the corresponding Σ_{dust} , each point implies a value of δ_{GDR} . We have assumed (Equation (2)) that a single δ_{GDR} describes each data set. A simple way to identify the α_{CO} that best fits this model is to try many α_{CO} and select the one that minimizes the scatter in $\log_{10} \delta_{\text{GDR}}$. First, we pick a set of α_{CO} that brackets the true value. For each α_{CO} , we calculate Σ_{gas} and combine it with Σ_{dust} to measure the rms scatter in $\log_{10} \delta_{\text{GDR}}$. This yields clear minima in each data set, which we identify as our best-fit α_{CO} .

We experimented with several other approaches, including plane fits with errors in all three axes. The results agree with what we report here except that the plane fit is less stable in the inner part of M 31, NGC 6822, and the northern part of the SMC. The presence of significant intrinsic scatter in the relation makes the weighting of data subjective and so the plane fit is not significantly more rigorous than using the scatter as a goodness-of-fit metric. We also experimented with maximization of the linear and rank correlation coefficients relating dust and gas. Most of these approaches yield similar results. Our uncertainty

estimates include substituting the median absolute deviation for the rms in the goodness of fit.

This method can fail in a data set without a good mix of H_2 and H I -dominated lines of sight. For example, in a data set with 100 overwhelmingly H I lines of sight and three mostly molecular lines of sight, the H I -dominated data will drive the scatter in $\log_{10} \delta_{\text{GDR}}$ leaving little sensitivity to α_{CO} . In such a case, we would like to weight the high H_2 lines of sight more heavily. In practice, our definition of sampling regions addresses this concern and we weight all points equally.

APPENDIX B

UNCERTAINTIES

We gauge the uncertainty in the best-fit α_{CO} in three ways. (1) We vary details of the calculation (the calibration and background for each map, the dust model, and the goodness-of-fit statistic) across their plausible range, repeating our solution for each new set of assumptions. (2) We solve for α_{CO} in a simulated noisy data set where we know the true α_{CO} by construction. (3) We repeat the original solution while bootstrapping, solving for α_{CO} using data drawn from the original sample (with the same number of elements) allowing repeats. We thus assess the sensitivity of α_{CO} to our assumptions, statistical uncertainty, and robustness. We bookkeep each as a gain-style uncertainty (i.e., rms in $\log \alpha_{\text{CO}}$) and then take our overall uncertainty to be the sum of all three terms in quadrature.

In the first test, we carry out 100 iterations. Although the Draine & Li (2007) models have been applied successfully to the SMC (Sandstrom et al. 2010), adopting them represents a key assumption. Therefore, in each iteration we randomly select with equal probability to use either the Draine & Li (2007) dust models or a modified blackbody with $\beta = 1\text{--}2$ and assuming 50% of the $70\text{ }\mu\text{m}$ emission to come from out-of-equilibrium very small grain emission, a value appropriate for the SMC

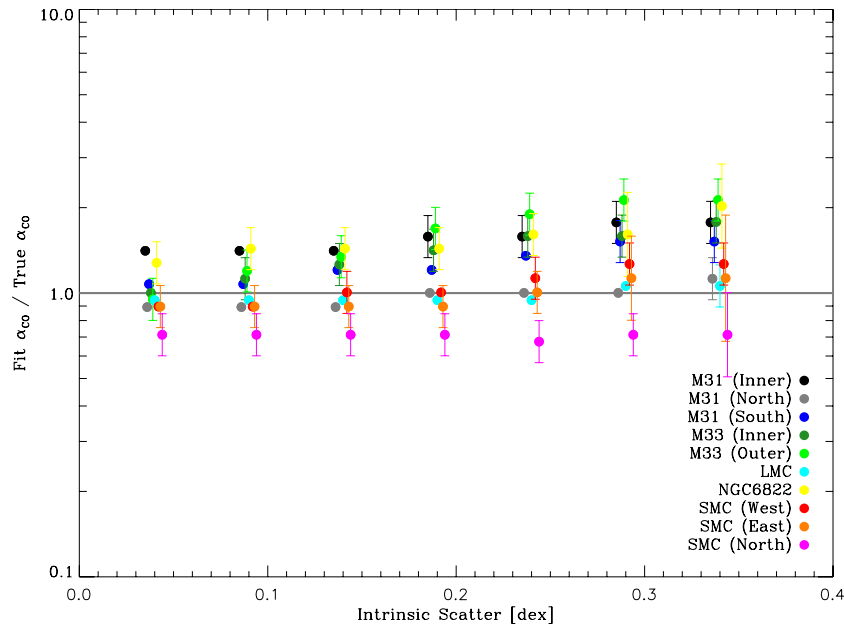


Figure 8. Fits to simulated data. The y-axis gives the mean best-fit α_{CO} divided by the true value (known by construction) as a function of the intrinsic scatter in the dust–gas relation (x-axis). Error bars show the rms scatter in the best-fit α_{CO} . The horizontal line at 1 shows a perfect match between true and best-fit α_{CO} . Different colors indicate different systems. For realistic intrinsic scatter ($\lesssim 0.2$ dex, see Table 2), we recover the true α_{CO} with better than 40% accuracy in all cases.

(Leroy et al. 2009). We also select our goodness-of-fit statistic to be with equal probability either the rms scatter (as in the main result) in $\log_{10} \delta_{\text{GDR}}$, the fractional scatter in δ_{GDR} , or the median absolute deviation in $\log_{10} \delta_{\text{GDR}}$. We randomize the zero point of the IR maps and the absolute calibration of each data set within their plausible value. Finally, we adjust the zero point of the H I map, either varying the assumed zero point by $\pm 20\%$ (in the SMC) or $\pm 5 M_{\odot} \text{ pc}^{-2}$ (in the other galaxies). In detail, we vary the zero points of the IR maps by typically ± 0.1 and 0.5 at 70 and $160 \mu\text{m}$ (1σ , this depends slightly on the target). We adjust overall scale of the CO and H I data by $\pm 15\%$ (1σ) and the IR maps by $\pm 10\%$. When we use a modified blackbody we pick β randomly from the range 1–2 (always using a single value) and take a fraction 0.5 ± 0.1 of the $70 \mu\text{m}$ emission to come from out-of-equilibrium emission and so neglect it in the calculation. Each realization corresponds to a reasonable set of assumptions and yields a valid solution for α_{CO} and δ_{GDR} , but we emphasize that *the results presented in the main text represent our best estimates*.

In the second test, we take $\Sigma_{\text{H I}}$ and I_{CO} for each data set, assume an α_{CO} , add intrinsic scatter to the relation, add noise, and then solve for α_{CO} . We first take the real H I and CO data and assume the best-fit values of α_{CO} from Table 2 to be correct. We convert I_{CO} to Σ_{H_2} and then apply the measured δ_{GDR} to derive a Σ_{dust} for each point. At this point, we have a plane in CO–H I–dust space that is perfectly described by a single α_{CO} and δ_{GDR} . We add lognormal scatter to each quantity (equally distributed among the three axes) and finally apply noise to each axis. This yields a realistic approximation of real data for which we know the true α_{CO} . We do not know the intrinsic scatter a priori, so we try a range of values from 0 to 0.4 dex, applying $1/\sqrt{3}$ times this value to each axis. We repeat the exercise several times for each scatter, resampling the original data (allowing repeats) and re-generating the noise.

Figure 8 shows the result of this test. The y-axis gives the best-fit α_{CO} divided by α_{CO} assumed for the simulation. The x-axis shows the amount of intrinsic scatter applied when

making the simulated data. Each point shows the mean and scatter for ~ 50 tests. The statistical uncertainty reported in Table 2 is the rms scatter (in the log) about the true α_{CO} for all trials with intrinsic scatter < 0.2 dex, a realistic value based on Table 2. It thus incorporates both the mild bias and scatter seen in Figure 8.

REFERENCES

- Abdo, A. A., et al. 2010, *ApJ*, **710**, 133
 Arce, H. G., & Goodman, A. A. 1999, *ApJ*, **512**, L135
 Bernard, J.-P., et al. 2008, *AJ*, **136**, 919
 Bloemen, J. B. G. M., Deul, E. R., & Thaddeus, P. 1990, *A&A*, **233**, 437
 Bloemen, J. B. G. M., et al. 1986, *A&A*, **154**, 25
 Bohlin, R. C., Savage, B. D., & Drake, J. F. 1978, *ApJ*, **224**, 132
 Bolatto, A. D., Jackson, J. M., & Ingalls, J. G. 1999, *ApJ*, **513**, 275
 Bolatto, A. D., Leroy, A. K., Rosolowsky, E., Walter, F., & Blitz, L. 2008, *ApJ*, **686**, 948
 Bolatto, A. D., et al. 2007, *ApJ*, **655**, 212
 Bot, C., Boulanger, F., Lagache, G., Cambr sy, L., & Egret, D. 2004, *A&A*, **423**, 567
 Bot, C., Boulanger, F., Rubio, M., & Rantakyro, F. 2007, *A&A*, **471**, 103
 Bot, C., et al. 2010, *A&A*, **524**, A52
 Boulanger, F., Abergel, A., Bernard, J.-P., Burton, W. B., Desert, F.-X., Hartmann, D., Lagache, G., & Puget, J.-L. 1996, *A&A*, **312**, 256
 Brinks, E., & Shane, W. W. 1984, *A&AS*, **55**, 179
 Cambr sy, L., Jarrett, T. H., & Beichman, C. A. 2005, *A&A*, **435**, 131
 Cannon, J. M., et al. 2006, *ApJ*, **652**, 1170
 Dame, T. M., Hartmann, D., & Thaddeus, P. 2001, *ApJ*, **547**, 792
 de Blok, W. J. G., & Walter, F. 2003, *MNRAS*, **341**, L39
 Deul, E. R., & van der Hulst, J. M. 1987, *A&AS*, **67**, 509
 Dickey, J. M., Mebold, U., Stanimirovi , S., & Staveley-Smith, L. 2000, *ApJ*, **536**, 756
 Downes, D., & Solomon, P. M. 1998, *ApJ*, **507**, 615
 Draine, B. T. 2009, *Cosmic Dust–Near and Far*, **414**, 453
 Draine, B. T., & Li, A. 2007, *ApJ*, **657**, 810
 Draine, B. T., et al. 2007, *ApJ*, **663**, 866
 Dufour, R. J. 1984, in *IAU Symp. 108, Structure and Evolution of the Magellanic Clouds*, ed. S. van den Bergh & K. S. D. de Boer (Cambridge: Cambridge Univ. Press), 353
 Dutra, C. M., Ahumada, A. V., Clari , J. J., Bica, E., & Barbuy, B. 2003, *A&A*, **408**, 287
 Dwek, E. 1997, *ApJ*, **484**, 779

- Dwek, E. 1998, *ApJ*, **501**, 643
- Engargiola, G., Plambeck, R. L., Rosolowsky, E., & Blitz, L. 2003, *ApJS*, **149**, 343
- Fukui, Y., & Kawamura, A. 2010, *ARA&A*, **48**, 547
- Fukui, Y., et al. 1999, *PASJ*, **51**, 745
- Glover, S. C. O., & Mac Low, M. 2010, *MNRAS*, **412**, 337
- Gordon, K. D., et al. 2005, *PASP*, **117**, 503
- Gordon, K. D., et al. 2006, *ApJ*, **638**, L87
- Gordon, K. D., et al. 2009, *ApJ*, **690**, L76
- Gordon, K. D., et al. 2010, *A&A*, **518**, L89
- Gratier, P., Braine, J., Rodriguez-Fernandez, N. J., Israel, F. P., Schuster, K. F., Brouillet, N., & Gardan, E. 2010, *A&A*, **512**, A68
- Grenier, I. A., Casandjian, J., & Terrier, R. 2005, *Science*, **307**, 1292
- Heyer, M., Krawczyk, C., Duval, J., & Jackson, J. M. 2009, *ApJ*, **699**, 1092
- Heyer, M. H., Corbelli, E., Schneider, S. E., & Young, J. S. 2004, *ApJ*, **602**, 723
- Hughes, A., et al. 2010, *MNRAS*, **406**, 2065
- Israel, F. P. 1997a, *A&A*, **317**, 65
- Israel, F. P. 1997b, *A&A*, **328**, 471
- Jenkins, E. B. 2009, *ApJ*, **700**, 1299
- Keller, S. C., & Wood, P. R. 2006, *ApJ*, **642**, 834
- Kim, S., Staveley-Smith, L., Dopita, M. A., Freeman, K. C., Sault, R. J., Kesteven, M. J., & McConnell, D. 1998, *ApJ*, **503**, 674
- Kim, S., Staveley-Smith, L., Dopita, M. A., Sault, R. J., Freeman, K. C., Lee, Y., & Chu, Y. 2003, *ApJS*, **148**, 473
- Leroy, A., Bolatto, A., Stanimirović, S., Mizuno, N., Israel, F., & Bot, C. 2007, *ApJ*, **658**, 1027
- Leroy, A. K., et al. 2009, *ApJ*, **702**, 352
- Lisenfeld, U., & Ferrara, A. 1998, *ApJ*, **496**, 145
- Liszt, H., Pety, J., & Lucas, R. 2010, *A&A*, **518**, A45
- Madden, S. C., Poglitsch, A., Geis, N., Stacey, G. J., & Townes, C. H. 1997, *ApJ*, **483**, 200
- Maloney, P., & Black, J. H. 1988, *ApJ*, **325**, 389
- Meixner, M., et al. 2006, *AJ*, **132**, 2268
- Mizuno, N., Rubio, M., Mizuno, A., Yamaguchi, R., Onishi, T., & Fukui, Y. 2001, *PASJ*, **53**, L45
- Montalto, M., Seitz, S., Riffeser, A., Hopp, U., Lee, C., & Schönrich, R. 2009, *A&A*, **507**, 283
- Muller, E., et al. 2010, *ApJ*, **712**, 1248
- Muñoz-Mateos, J. C., et al. 2009, *ApJ*, **701**, 1965
- Nieten, C., Neininger, N., Guélin, M., Ungerechts, H., Lucas, R., Berkhuijsen, E. M., Beck, R., & Wielebinski, R. 2006, *A&A*, **453**, 459
- Pak, S., Jaffe, D. T., van Dishoeck, E. F., Johansson, L. E. B., & Booth, R. S. 1998, *ApJ*, **498**, 735
- Pineda, J. E., Caselli, P., & Goodman, A. A. 2008, *ApJ*, **679**, 481
- Pineda, J. L., Ott, J., Klein, U., Wong, T., Muller, E., & Hughes, A. 2009, *ApJ*, **703**, 736
- Roman-Duval, J., et al. 2010, *A&A*, **518**, L74
- Rosolowsky, E., Engargiola, G., Plambeck, R., & Blitz, L. 2003, *ApJ*, **599**, 258
- Rosolowsky, E., Keto, E., Matsushita, S., & Willner, S. P. 2007, *ApJ*, **661**, 830
- Rosolowsky, E., & Simon, J. D. 2008, *ApJ*, **675**, 1213
- Rubio, M., Boulanger, F., Rantakyro, F., & Contursi, A. 2004, *A&A*, **425**, L1
- Rubio, M., Lequeux, J., & Boulanger, F. 1993, *A&A*, **271**, 9
- Rupke, D. S. N., Veilleux, S., & Baker, A. J. 2008, *ApJ*, **674**, 172
- Sandstrom, K. M., Bolatto, A. D., Draine, B. T., Bot, C., & Stanimirović, S. 2010, *ApJ*, **715**, 701
- Schlegel, D. J., Finkbeiner, D. P., & Davis, M. 1998, *ApJ*, **500**, 525
- Schnee, S. L., Ridge, N. A., Goodman, A. A., & Li, J. G. 2005, *ApJ*, **634**, 442
- Solomon, P. M., Rivolo, A. R., Barrett, J., & Yahil, A. 1987, *ApJ*, **319**, 730
- Stanimirovic, S., Staveley-Smith, L., Dickey, J. M., Sault, R. J., & Snowden, S. L. 1999, *MNRAS*, **302**, 417
- Stepnik, B., et al. 2003, *A&A*, **398**, 551
- Strong, A. W., & Mattox, J. R. 1996, *A&A*, **308**, L21
- Tabatabaei, F. S., Beck, R., Krügel, E., Krause, M., Berkhuijsen, E. M., Gordon, K. D., & Menten, K. M. 2007, *A&A*, **475**, 133
- Thronson, H. A., Jr. 1988, in *NATO ASIC Proc. 232, Galactic and Extragalactic Star Formation*, ed. R. E. Pudritz & M. Fich (Dordrecht: Kluwer), 621
- Tumlinson, J., et al. 2002, *ApJ*, **566**, 857
- Verley, S., Hunt, L. K., Corbelli, E., & Giovanardi, C. 2007, *A&A*, **476**, 1161
- Walter, F., et al. 2007, *ApJ*, **661**, 102
- Wilson, C. D. 1995, *ApJ*, **448**, L97
- Wolfire, M. G., Hollenbach, D., & McKee, C. F. 2010, *ApJ*, **716**, 1191
- Yin, J., Hou, J. L., Prantzos, N., Boissier, S., Chang, R. X., Shen, S. Y., & Zhang, B. 2009, *A&A*, **505**, 497
- Zhukovska, S., Gail, H.-P., & Tieloff, M. 2008, *A&A*, **479**, 453